Measurement of induced currents in radio frequency magnetic fields based on near field antenna perturbations

J. M. Jennings ⓘD, A. Kar ⓘD, and R. Vaidyanathan

COLLECTIONS

View Online   Export Citation   CrossMark

ARTICLES YOU MAY BE INTERESTED IN

Periodic orbits, superintegrability, and Bertrand's theorem
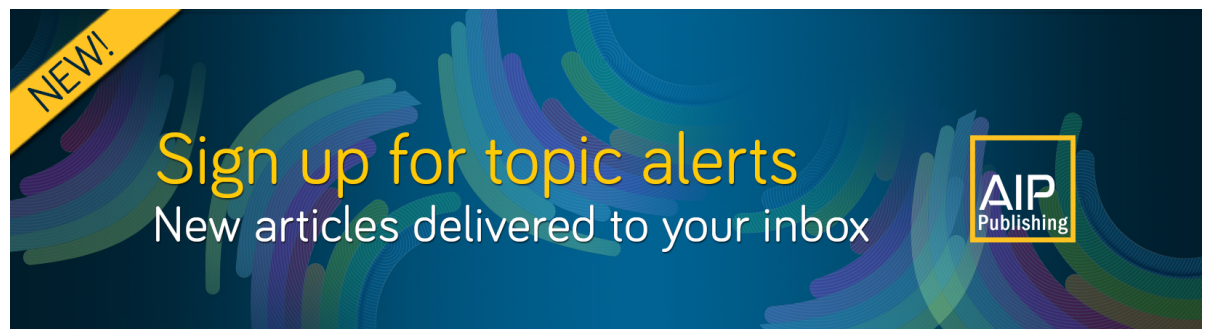AIP Advances **10**, 065003 (2020); https://doi.org/10.1063/1.5143582

Geometric optimization of plasmonic nanostructure arrays on MWIR HgCdTe (MCT)
AIP Advances **10**, 065006 (2020); https://doi.org/10.1063/1.5136253

Surfactant-free, UV-curable core–shell microcapsules in a hydrophilic PDMS microfluidic device
AIP Advances **10**, 065101 (2020); https://doi.org/10.1063/5.0004736

Measurement of induced currents in radio frequency magnetic fields based on near field antenna perturbations

View Online   Export Citation   CrossMark

J. M. Jennings,[1,a] 🔵 A. Kar,[2] 🔵 and R. Vaidyanathan[3]

AFFILIATIONS

[1] Materials Science and Engineering, University of Central Florida, Orlando, Florida 32816, USA

[2] Laser-Advanced Materials Processing Laboratory, Center for Research and Education in Optics and Lasers (CREOL),
College of Optics and Photonics, University of Central Florida, Orlando, Florida 32816, USA

[3] Advanced Materials Processing and Analysis Center (AMPAC), Materials Science and Engineering,
Mechanical and Aerospace Engineering, University of Central Florida, Orlando, Florida 32816, USA

[a] **Present address:** L3Harris Technologies, Inc., 1025 W. Nasa Boulevard, Melbourne, FL 32919, USA.
Author to whom correspondence should be addressed: jeffreymjennings@knights.ucf.edu

ABSTRACT

A measurement system is developed utilizing electromagnetic compatibility test equipment for the study of induced current in conductive materials subjected to radio frequency (RF) magnetic field strengths similar to the 1.5 T magnetic resonance imaging (MRI) B_1 magnetic field at ~65 MHz. The intent of developing such a system was to produce μT range RF magnetic fields in the laboratory to facilitate characterization of induction in conductive materials with modified surface electromagnetic properties to address unintended eddy current issues like Joule heating caused by implanted devices during MRI. A Helmholtz coil (HHC) is used as the RF magnetic field source, and the radiated field is monitored using a receiving loop antenna positioned coaxially outside the HHC. The measurement system operates in continuous wave and pulsed wave modes. Analytical models of the system were derived, which calculate the spatial distribution of RF magnetic flux and the induced current within a coaxially located sample in the transmission path between the HHC and receiving (R/C) loop from output voltage measurements at a single coaxial position. Induced currents were evaluated at multiple flux densities and at different frequencies, showing direct proportionality over the flux densities tested. Induced current results recorded in samples of different sizes and electrical conductivities (ranging from 0.1 to 5.8×10^7 $(\Omega$ m$)^{-1}$ produced changes, matching trends predicted by conductive, closed-loop antenna theory. Induced currents were also used with simultaneous temperature rise measurements to characterize the effective surface conductivity for wire with non-uniform properties at 65 MHz.

I. INTRODUCTION

Unintended induction remains a major challenge in environments where conductors are exposed to radio frequency (RF) magnetic fields. Eddy currents due to the proximity of adjacent active RF circuits are a major source of electromagnetic interference (EMI) within electronic devices, causing degraded performance, unwanted Joule heating, and potential electrical/thermal overstress.[1] A similar unintended RF induction arises in electrical circuits during solar storms or following exposure to electromagnetic pulses.[2] An environment where the consequences of unplanned eddy current generation are particularly severe is inside a patient with implanted medical devices (e.g., pacemaker leads, deep brain stimulation probes, etc.) constructed from conductive materials during magnetic resonance imaging (MRI).[3–11]

During MRI, three superimposed magnetic field components are present: (1) the static, high strength field, B_o; (2) the pulsed gradient field (kHz frequencies); and (3) the pulsed, circularly polarized RF field, B_1.[3] The RF carrier frequency of the B_1 field is related to B_o by the Larmor frequency relation (42.58 MHz/T for hydrogen)

and varies from 9 to nearly 400 MHz for MRI systems for B_o field strengths ranging from 0.2 T to 9.4 T, with future increase likely as MRI research drives the available B_o field strengths to 20 T and beyond.[4,10–12] Other key parameters for the B_1 RF magnetic field include pulse shape, peak amplitude, and pulse repetition rate (i.e., repetition time).[4] For example, a typical 1.5 T imaging sequence may apply a pulsed sinc function signal reaching a peak RF magnetic field strength, B_{1-peak}, of up to 30 μT (~6 μT to 8 μT rms at 10–20 ms repetition time).[4] When electrically conductive materials like those commonly used in the construction of implanted medical devices are exposed to these imaging conditions, the B_1 fields orthogonal to the device, due to their time varying nature, induce currents.[13] The extent of those currents differs based on the RF magnetic field strength and frequency, as well as the properties, geometry, and orientation of the unintentional current pathways that form within the implanted device or between itself and its adjacent organic tissue.[14] These currents are known to produce imaging artifacts and Joule heating in tissues adjacent to the implants.[3,7]

Recently, the tailoring of the electromagnetic (EM) surface properties of the conductors used in implant construction to influence their RF magnetic field interaction has been studied as a potential avenue to mitigate the implanted device's Joule heating effects.[15,16] Since the skin effect limits the RF magnetic field interaction to a conductor's surface, surface EM property alterations can provide beneficial effects like increased EM reflection while preserving favorable bulk material properties. When assessing the changes introduced by different surface property modifications to B_1 field interactions, relating the eddy currents generated to those properties in simple structures provides an effective measure since it decouples the induced current response from many of the device specific geometry and orientation effects. A combination with temperature rise measurements further enables relating induced currents with surface EM properties (specifically electrical conductivity, σ, for non-magnetic materials) to provide differentiation from bulk properties, which is not possible using traditional direct current characterization techniques.

When the interactions of B_1 fields with implanted devices are studied, a common experimental approach utilizes *in vitro* "phantom" testing in an operational or simulated MRI system similar to the test method documented in ASTM Standard F2182-11a.[17] Stand-alone medical implant test systems (e.g., Zurich Med Tech's MITS1.5) also exist, which accurately reproduce RF B_1 field conditions for the safety evaluation of new implanted medical devices. While both of these methods are highly effective for the evaluation of specific device configurations, limited access and their high cost can inhibit research related to B_1 field–conductor interactions. In addition, the complex interactions occurring within an MRI imaging chamber make the application of uniform RF magnetic fields over a sample geometry and analytical analysis of results challenging, particularly at higher frequencies.[18] As a result, when considering the fundamental study of material surface EM property effects on induction when exposed to RF magnetic fields, like the B_1 fields applied during MRI, a measurement system able to uniformly apply RF magnetic fields at comparable frequencies and flux densities to the B_1 field has utility.

Since no existing equipment meets these requirements, a novel measurement system is assembled utilizing a unique combination of antenna structures, transmitters, receivers, and analytical equipment

which produces inductive RF magnetic fields similar to the aforementioned B_1 field conditions. The ensemble is described in detail, and its generated RF magnetic fields are characterized and compared with typical 1.5 T MRI B_1 field levels. An analytical model of the test configuration is derived, which relates the measured data to the currents present within the various antenna elements including the conductive material sample being evaluated. The measurement system is applied to evaluate the magnetic field strength-to-induced current relationships for material samples fabricated from different known non-magnetic, conductive materials based on antenna output measurements across the RF magnetic fields of interest and in combination with simultaneous temperature rise measurements; the current results are used to estimate the effective surface conductivity of a material sample with conductivity variations occurring within its skin depth of the wire at 65 MHz.

II. RF MAGNETIC INDUCTION SYSTEM

The measurement system takes advantage of the perturbation in the received signal that occurs when a conductive material with induced currents is placed in between a RF magnetic field source and a receiving antenna inside the near-field region of the source. The induced free electron flow within a conductive, closed-loop shields the receiving antenna downstream, reducing its detected RF magnetic field. This effect has previously been utilized in antenna applications consisting of concentric arrays of parasitic and active loop antennas to improve antenna directionality.[19] The radiating RF magnetic field source utilized in the current experiment is a shielded Helmholtz coil (HHC). HHCs are characterized by the very uniform unidirectional magnetic field along their central axis produced between the parallel loop antennas (see Fig. 1). In this measurement system, the HHC provides a compact means of generating high RF magnetic flux densities not readily achievable using only a single radiating loop. Since the eddy currents generated within a conductor are proportional to the orthogonal component of the RF magnetic field independent of field polarization, the polarization differences between the HHC's linear RF field and the circular MRI B_1 fields should not alter the eddy current–inductive RF field strength relationship. The specific HHC (HHS 1 + 1, Schwarzbeck Mess Elektronik) used consists of a custom-developed, split-fed parallel coaxial set of circular shielded single-loop antennas separated by a distance equal to the loop radius resonantly tuned to transmit its maximum field strength at ~65 MHz, a value matching the carrier RF frequency used in typical 1.5 T MRI systems.[3] The transmitted field strength is measured using a passive magnetic receiving (R/C) loop antenna (HFRAE 5163, Schwarzbeck Mess Elektronik) with an operating RF frequency range from 9 kHz to 300 MHz. The shielding configuration of the R/C loop antenna and HHC suppresses capacitive effects during measurements. The R/C loop magnetic antenna factor vs frequency calibration data are used to convert measured peak voltage and power values into the desired magnetic field strength.

A. Experimental setup

For all measurements, the R/C loop antenna and conductive loop sample are placed coaxially and in parallel to the HHC loops to maximize the orthogonal component of the RF magnetic field
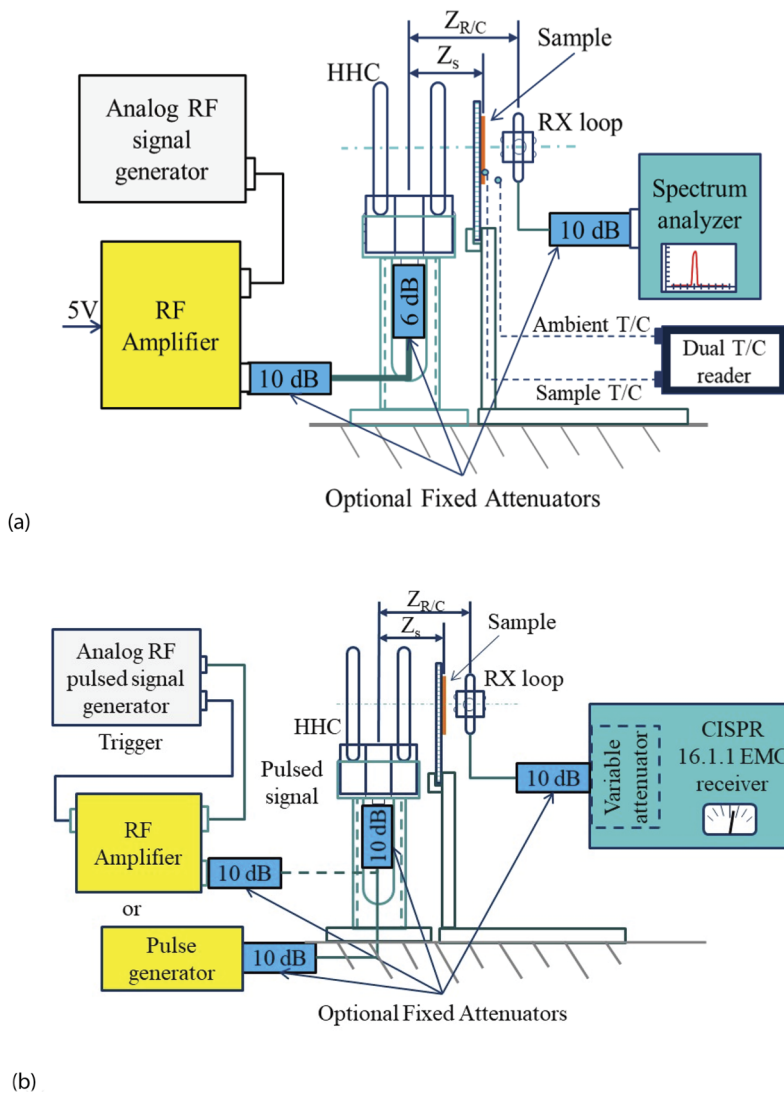
(a)

(b)

FIG. 1. Schematic view of the induced current measurement experimental setup for two operating modes: A) the continuous wave mode (CW) with thermocouples (T/C) for temperature rise characterization and B) the pulsed wave mode.

applied to the sample loop under evaluation. Stands support the HHC, sample, and R/C coil coaxially when in the test configuration and allow each to move independently to change their relative separation. The stands are constructed of low dielectric materials (acrylic, PVC, and wood) to minimize their effects on the transmitted RF magnetic field. The R/C coil output cable is oriented at 90° to the HHC split feed to enable measurement of the field strength in the middle of the HHC. The measurement system consists of a signal source used to drive the HHC loops, an HHC loop transmitting antenna, a sample and holder, an R/C loop antenna, and a receiver used to measure the output from the R/C loop antenna.

Two system configurations, or modes, are described: continuous wave (CW) and pulsed wave based on the nature of the RF field source used. Schematic views of both are shown in Fig. 1. The CW mode uses a harmonic, constant-amplitude wave source and provides a means for studying conductive material interactions with RF

magnetic fields decoupled from transient pulse shape effects. The pulsed wave mode provides either a narrow broad-spectrum pulse or shaped pulse superimposed with the RF carrier frequency cycled at repetition times able to match a particular MRI sequence being simulated.

During CW mode testing, the HHC is driven using a signal generator (MXG-AT-N5181A, Agilent Technologies) to produce a sine wave at the desired RF frequency and amplitude that is routed to a 30-W RF amplifier (3900-1, Herley-Lancaster) capable of providing 59 ± 3 dB of CW amplification. The high-power output of the amplifier is connected to the HHC using a 50 Ω (305 cm-long, LMR-400) cable. The R/C loop antenna output is measured using a spectrum analyzer (AT-N9320B/PA3, Agilent Technologies) yielding power readings in dBm based on the average of 100 readings. Fixed attenuators were optionally placed in the transmission and receiving path to control the power signal level and improve the voltage standing

wave ratio (VSWR) between the amplifier and the HHC. The fast Fourier transform measured peak from the spectrum analyzer provides the magnitude of the measured signal, which is converted to magnetic field strength by summing the loop antenna conversion factor and receiving path in-line attenuation values to the measured peak power converted to dB μV. In the CW mode, temperature rise is determined using thermocouples (T/Cs): one in contact with the sample to measure its steady-state temperature rise and the other positioned in close proximity to measure the ambient temperature conditions adjacent to the sample and any Joule heating associated with induced current within the T/C circuit.

The pulsed wave mode experimental configuration drives the HHC alternately with either a pulse generator (IGUF 2910 S, Schwarzbeck Mess Elektronik) with a custom pulse repetition frequency of 50 Hz and a peak field strength at the HHC center of ~14 μT for pulsed mode characterization purposes or with an RF signal generator with an internal trigger (SMC100A, Rohde and Schwarz) combined with the up to 300-W pulsed RF amplifier for high field strength testing up to 30 μT and beyond. In-line fixed attenuators are included at the output of the pulse generator or amplifier and input to the HHC for most measurements to control output power and improve impedance matching within the 50 Ω coaxial connection. The output of the R/C loop antenna is connected via a 50 Ω (305 cm-long, LMR-400) cable coaxial cable with inline fixed attenuation for receiver protection to an International Special Committee on Radio Frequency Interference (CISPR) 16.1.1 Standard electromagnetic compatibility (EMC) receiver (FCVU-1534, Schwarzbeck Mess Elektronik) used for pulsed peak field strength measurements. The EMC receiver is optimized for detecting short pulse signals and provides a pulse width-dependent weighted output related to the peak detected field strength displayed in dB μV.[20] Through the use of its internal variable attenuator, the input amplitude is tuned into the most sensitive region of the receiver display (0–5 dB μV), allowing measurements to the closest $\frac{1}{4}$ dB μV in the linear region or $\frac{1}{2}$ dB μV in the logarithmic region. The measured peak voltage is converted to peak magnetic field strength by summing it with the R/C loop signal-to-magnetic field strength conversion value and a CISPR weighting factor, $CISPR_{WF}$.

B. Weighting factor determination

In typical CISPR 16.1.1 EMC characterizations, the specified limits being evaluated are defined in terms of the weighted receiver output, so knowledge of the CISPR weighting factor is not needed.[20] In the current measurement system, however, where the absolute peak voltage is sought, the pulse width-to-weighting factor relationship is required. The pulse width dependence of $CISPR_{WF}$ was determined by injecting pulsed signals with known peak voltages directly from the RF signal generator into the EMC receiver and recording the effect of varying pulse width on the reading. This result is shown in the lower right region of the plot in Fig. 2.

As the pulse width is reduced, the magnitude of the weighting factor gradually increases linearly with the log of the pulse width until ~0.05 ms where there is a drastic slope change as the minimum pulse width is reduced to the limit of the RF analog signal generator (0.001 ms). Since this pulse width range does not overlap the narrow pulse width (~10^{-7} ms) output from the pulse generator, the weighting factor value is predicted by linearly extrapolating the slope of
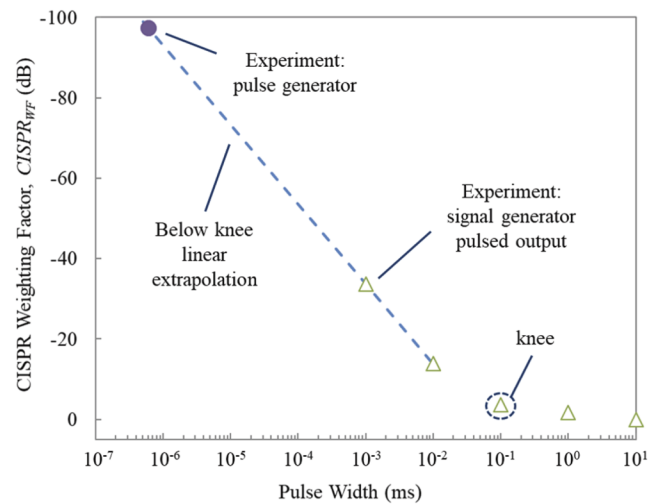

FIG. 2. $CISPR_{WF}$ (dB) vs input signal pulse width (ms) for the RF analog signal generator (control) compared with IGUF 2910 S pulse generator output.

the measured results found beyond the knee into the narrower pulse width range. The $CISPR_{WF}$ factor for the pulse generator is estimated from the measured pulse generator output voltage $V_{PG}(t)$ through a 50 Ω load in the time domain. Its output consists of a peak instantaneous voltage of 263 V and a pulse width of the high pulse region of ~6.1×10^{-7} ms. The difference between this instantaneous voltage value converted to dBm and the measured result of the EMC receiver is −97.51 dB. This estimate agrees well with the value predicted by the linearly extrapolated measured pulse generator weighting factor results, as shown in Fig. 2.

C. Analytical model

Traditionally, experiments utilizing HHCs are conducted between the two driven loops in the region with a nearly constant RF magnetic flux. In this case, the measured results are produced with the sample and R/C loop positioned outside the HHC where the axial magnetic field strength decays rapidly as the separation from the coils increases. Comparison of the field strength values at the R/C loop with and without the sample provides a measurement which can be used to analytically determine the current flowing within a conductive, closed-loop sample. Since the separation from the source to receiving elements is comparable to the loop sizes, an analytical model representing the experiment must account for the phase differences caused by the separation variation between current elements located around the perimeter of the 2 HHC source loops to points on the sample and receiving loops where currents are induced. For this analysis, the geometry of the loop antennas and samples within the system meet the small-thin loop criteria: (1) the square of the wire radius is significantly less than the square of the loop radius, and (2) the magnitude of the product of the loop radius and the wavelength constant, β, ($\beta = 2\pi/\lambda$ for the input signal frequency free space wavelength, λ) is $\gg$1, which enables the following simplifying assumptions: (1) the current remains constant around the circumference of each loop, and (2) the wire radius is sufficiently

small with respect to the given loop radius for its effects on the separation to be neglected.[21] Applying these simplifying assumptions to the experimental setup results in the model shown in Fig. 3 as described.

For the representation shown in Fig. 3, the field strength magnitude sensed by the R/C loop is assumed to be the superposition of the magnetic flux magnitudes generated by the other loops within the array. This quantity, determined from antenna output measurements, can be related to the source current values, I_i, within each array loop by leveraging the analytical approach previously developed for a single source loop and receiving loop pair.[22] This near-field model modifies Faraday's law of induction to relate the voltage induced at the terminals of the R/C loop, $V_{R/C}$ (the measured quantity), with the magnetic flux produced by a single transmitting loop antenna, $B_{ave,R/C}(z)$, as follows:

$$V_{R/C} = -j\omega_n \vec{B}_{ave,R/C}(z) \cdot \vec{S}_{R/C}, \tag{1}$$

where ω_n is the harmonic radial frequency of the input (in radians/s), $j = \sqrt{-1}$, $S_{R/C}$ is the area of the R/C loop, and $B_{ave,R/C}(z) = \mu_o H_{ave,R/C}$, where μ_o, the permeability of free space, is $4\pi x 10^{-7}$ H/m, and $H_{ave,R/C}$ is the average free-space magnetic field strength within the area of the R/C loop (A/m). According to this analysis, the field contribution of each source loop, $H_{ave,i-R/C}$, to the field strength at the R/C loop is related to the current within the source loop, i, by the following equation:

$$H_{ave,i-R/C}(z) = -j\frac{\beta I_i r_i}{r_{R/C}} \sum_{m=0}^{\infty} \frac{1}{(2m+1)!} \frac{1 \times 3 \times 5 \dots 2m+1}{2 \times 4 \times 6 \dots 2m+2}$$
$$\times \left[\frac{\beta r_i r_{R/C}}{R_{i-R/C}}\right]^{2m+1} h_{2m+1}^{(2)}(\beta R_{i-R/C})$$
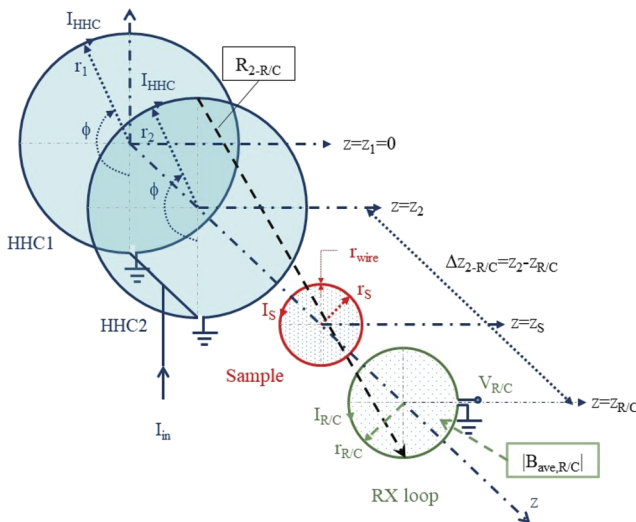$$= GF_{i-R/C}(z)I_i \tag{2}$$

FIG. 3. Analytical model of the loop array experimental configuration (shown with the sample present).

where I_i is the current in the source loop, i (A), r_i is the radius of the source loop (m), $R_{i-R/C}(z) = (r_i^2 + \Delta z_{i-R/C}^2 + r_{R/C}^2)^{1/2}$ is the maximum distance from a current element on the source loop, i, to a point on the R/C loop (m), and $h_{2m+1}^{(2)}(\beta R_{i-R/C})$ is the spherical Hankel function of the second kind dependent on the product of the wave number and separation. For the current measurement system, summing the first 20 terms proved sufficient to achieve the desired convergence in the value of $GF_{i-R/C}(z)$. The HHC loop currents, $I_{HHC}(z)$, assumed to be equal are calculated from the measured magnetic field strength with no sample present using the following equation:

$$I_{HHC}(z) = \frac{\left|H_{ave,R/C,ns}(z)\right|}{\left|GF1_{HHC1-R/C}(z) + GF1_{HHC2-R/C}(z)\right|}. \tag{3}$$

When estimating the spatial distribution of the magnetic flux along the z axis outboard of the HHC loops, $I_{HHC}(z)$ is found using Eq. (3) at a reference plane located at z_{ref}. The expected field strength, $H_{ave,R/C,ns}(z)$, is calculated for values of z across the spatial separation range of interest using the following equation:

$$\left|H_{ave,R/C,ns}(z)\right| = I_{HHC}(z_{ref})\left|GF1_{HHC1-R/C}(z) + GF1_{HHC2-R/C}(z)\right|. \tag{4}$$

The induced current within the conductive, closed-loop sample, $I_s(z)$, is found from the difference between the field strength contributions to the no-sample field strength, $H_{ave,R/C,ns}(z)$, and the with-sample field strength, $H_{ave,R/C,s}(z)$, as shown in the following equation:

$$I_s(z) \cong \frac{\left|H_{ave,R/C,s}(z_s)\right| - \left|H_{ave,R/C,ns}(z)\right|}{\left|GF1_{s-R/C}(z)\right|}. \tag{5}$$

This current magnitude was utilized in the thermal model developed by Barletta and Zanchini for steady-state temperature rise in a resistive cylinder conducting an RF current.[23] Via inspection, the model reveals that the effective electrical conductivity within the conductor's skin depth is proportional to $\Delta T^2/I_s(z)^4$, where ΔT is the difference between the measured initial and steady state temperature achieved at the conductor surface when exposed to an inductive RF field.

D. Closed-loop sample preparation

The conductive, closed-loop samples were formed by wrapping round wire around a cylindrical dowel, twisting the ends together and soldering the ends together to provide the electrical connection needed to achieve closure, as shown in Fig. 4.

The solder alloy and flux combinations used to close the loop are based on the metallurgical requirements for the specific wire material. Samples with different loop sizes and wire diameters were fabricated using non-magnetic (relative permeabilities near 1.0) conductors with electrical conductivities ranging from 0.1–5.8 × 10⁷ 1/Ω m to assess the detectability of sample electromagnetic property effects on the induced current. Also included was a wire sample with different surface and bulk properties, ~2 μm thick Sn-plated Cu wire, to assess the ability of the proposed measurement system to

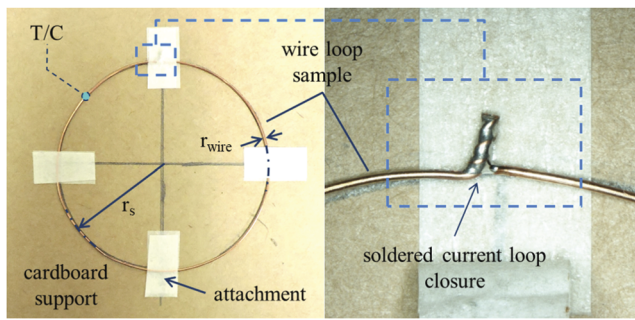**FIG. 4**. Closed wire loop sample with the approximate thermocouple (T/C) location identified.

$$CW : \left| H_{ave,R/C} \right|_{dB\ \mu A/m} = \left| P_{peak-SA} \right| + 90 + 10 \log Z_{in}$$
$$+ A_{RX} + AF_{RX}, \tag{6}$$

$$Pulsed : \left| H_{ave,R/C} \right|_{dB\ \mu A/m} = \left| V_{reading\text{-}QP} \right| + A_{Var} + A_{RX}$$
$$+ CISPR_{WF} + AF_{RX}, \tag{7}$$

where $\left| P_{peak\text{-}SA} \right|$ is the peak power reading from the spectrum analyzer at the frequency of interest (in dBm), Z_{in} is the RF circuit impedance (50 Ω), A_{RX} is the total value of fixed attenuators in the signal path from the RX loop antenna and the receiver, AF_{RX} is the calibrated magnetic antenna factor at the measurement frequency, $\left| V_{reading\text{-}QP} \right|$ is the meter reading on the EMI receiver in the quasi-peak (QP) mode (in dB μV), A_{Var} is the variable input attenuator setting on the EMI receiver used to tune the meter into the linear region in dB, and $CISPR_{WF}$ is the QP weighting factor, which is discussed in Sec. II B. The AF_{RX} values for the frequencies tested are listed in Table II.

Effects of reference plane selection on model accuracy were also assessed. Measurement locations included the center of the HHC, potential sample positions, and other locations outboard of the HHC loops extending to a distance where the transmitted signal strength drops below detectable levels. Antenna output measurements for determination of field strengths were also taken at frequencies across the HHC bandwidth from 31 MHz to 100 MHz to allow for comparison with the expected HHC output.

Induced currents in the conductive, closed-loop samples were determined by measuring the R/C loop outputs with and without the sample located within the coaxial array between the HHC and R/C loops, as shown in Fig. 3, at a known distance from the R/C loop. CW measurements were at 55 MHz, 65 MHz, and 85 MHz, and the signal generator input power levels and attenuator configurations selected based on achieving RF magnetic flux densities were similar to the 1.5 T MRI B_1 RF magnetic field environment described previously. Simultaneous steady-state temperature rise and induced

differentiate surface and bulk electrical conductivities. The average loop radius, r_s, for each sample is determined by averaging multiple diameter measurements taken at locations around the circumference of the sample loop. The materials and dimensions of the samples characterized using the current measurement system are listed in Table I.

E. Measurement system characterization

To verify the capability of the measurement system to produce RF magnetic field strengths similar to 1.5 T MRI B_1 field levels and the ability of the analytical model to predict the HHC field distribution, voltage measurements at various R/C loop locations, input power levels, and frequencies were conducted in both CW and pulsed wave test modes. These results were converted to field strength to determine the sample region where the desired RF magnetic field strength generation was possible. The conversion of power or voltages to magnetic field strength (in dB μA/m) for both modes is given in the following equations:

TABLE I. Conductive, closed-loop sample properties.

Material grade	Typical conductivity ($\times 10^7$ 1/Ω m)	Loop closure solder materials	Wire radius, r_{wire} (mm)	Sample name	Average radius, r_{loop} (mm)
Copper, bright, conductive	5.65–5.8	63Sn/37Pb solder, ROL0 flux	0.255	Thick Cu 1	29.10
				Thick Cu 2	21.23
				Thick Cu 3	16.23
			0.064	Thin Cu 1	28.98
				Thin Cu 2	21.07
				Thin Cu 3	16.02
Aluminum, AL 1100	3.45–3.8	96 Sn/4Ag solder, superior no. 1260 flux	0.247	Thick Al 1	29.10
70/30 brass	1.50–1.62	63Sn/37Pb solder, ROL0 flux	0.253	Thick brass 1	29.02
302/304 stainless steel	0.14	91Sn/9Zn, superior no. 78 flux	0.248	Thick S.S. 1	29.07
Sn-plated Cu	0.92 – Sn 5.65–5.8 - Cu	63Sn/37Pb solder, ROL0 flux	0.253	Thick Sn–Cu 1	28.91

TABLE II. R/C loop magnetic antenna factor used in conversion of measured signals to magnetic field strengths.

Var.	R/C loop magnetic antenna factor (dB/Ω m) @ frequency, f (MHz)									
f	31	45	55	60	65	68	70	75	85	100
AF_{RX}	25.010	24.885	24.840	24.860	24.900	24.912	24.920	24.930	24.820	24.600

current measurements were then conducted near 14 μT (10 μT$_{rms}$) at 65 MHz to establish the induced current to electrical conductivity relationship for known material samples which are then used to estimate the effective surface conductivity for the Sn-plated Cu wire with different surface and bulk values.

III. EXPERIMENTAL RESULTS AND DISCUSSION

Measured flux densities at different R/C loop positions along the HHC center axis for the input signal power levels, (1) −16 dBm CW input signal and no fixed attenuator between the RF amplifier and HHC and (2) the pulse generator with fixed 10 dB attenuators at its output and at the HHC input, are shown in Fig. 5. The continuous curves shown in Fig. 5 represent the predicted distribution of the RF magnetic flux for these two cases found using Eq. (4). Experimental results recorded at various locations show reasonable repeatability with standard deviations of 0.41 dB for the pulsed case and 0.73 dB for the CW case. The detectability limit for low strength pulsed signals occurs at ~15.62 cm from the HHC center and corresponded to a flux density of ~0.1 μT. Two target flux density levels are identified, ~6 μT$_{ms}$ and 30 μT$_{peak}$, which represent the typical average and maximum strength levels associated with modern 1.5 T MRI. Also highlighted is 10 μT$_{rms}$ (14 μT$_{peak}$) for a sinusoidal CW signal with peak fields matching the earlier generation MRI peak B_1 signal strengths in which many of the Joule heating issues were originally identified.[3]

As Fig. 5 indicates, the predicted distributions of magnetic flux for both cases evaluated show a maximum that coincides with the inward edge of the HHC coil; then, an initially rapid decay that becomes more gradual as the distance from the HHC center is increased is shown. Comparison of the pulsed generator experimental data and the predicted distribution determined using the HHC center as the reference plane shows excellent agreement across the entire distance shown. At lower input levels, similar agreement is observed in the CW mode. As the input signal strength rises, however, the deviation between the HHC center-based distribution prediction and measured results increases. Shifting the reference plane to 7.62 cm for the CW case brings the modeled distribution and measurements back into agreement. This difference in outcomes suggests that at higher magnetic flux densities, the receiving path may become fully saturated and deviate from linearity in its response to the input signal. The CW mode results approach 30 μT at the HHC center and exceed 6 μT$_{rms}$ (8.5 μT$_{peak}$) out to ~7.5 cm from the HHC center. Thus, a position of 5.72 cm from the HHC center was selected as the sample location during induced current measurements. Experimental and modeled results for this location for the CW case across the frequency band of the HHC are shown in Fig. 6.

As Fig. 6 indicates, the modeled distributions based on Eq. (4) using the 7.62 cm reference plane continue to show good agreement with experimental results at each frequency, but there is a significant difference between the measured signal strength and the value predicted by summing the input signal strength with the antenna gain calibration information provided for the HHC. The periodic
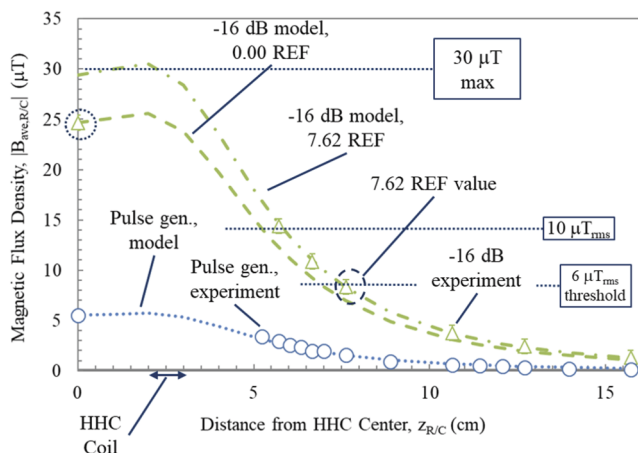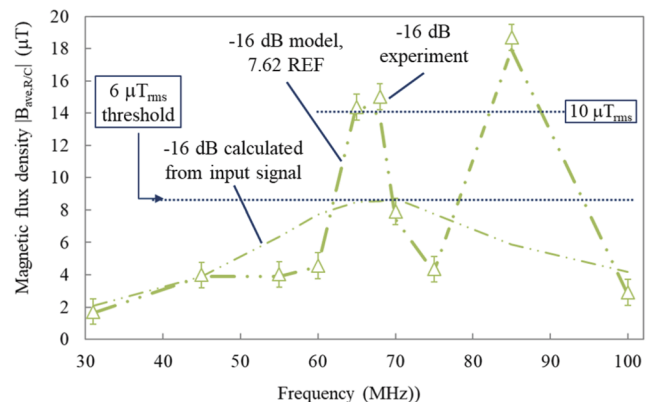

FIG. 5. Comparison of the predicted (lines) and measured (symbols) magnetic flux density amplitude results vs distance from the 10-cm diameter HHC center for different test modes: continuous wave −16 dB input with no fixed attenuators and pulsed wave with two 10 dB attenuators.

FIG. 6. Comparison of the expected magnetic flux distribution estimated from input signal properties, predicted from the reference plane at 7.62 cm measured field strength and measured magnetic flux density amplitude results vs frequency at the selected sample location 5.72 cm from the HHC center.

nature of this difference indicates the existence of a VSWR inter-action occurring within the input path to the HHC, which results in constructive and destructive interference across the frequency range tested with a period of ~20 MHz. The addition of attenua-tors at the RF amplifier output and at the HHC input line reduces the effect but also reduces the maximum flux density possible. Tak-ing advantage of this interaction, the value of 10 μT_{rms} (14 μT_{peak}) flux density is achieved at frequencies from 65 MHz to 68 MHz, which exceeded at 85 MHz but dropped well below that level over most frequencies. The close agreement between experimental data and modeled distributions presented in Figs. 5 and 6 provides val-idation for the superposition assumption and confirms the ability to accurately predict the magnetic field strengths at different loca-tions outside of the HHC for both CW and pulsed RF magnetic fields, when based on an appropriately selected reference plane mea-surement. This ability is essential in determining the strength of the RF magnetic fields applied to the sample during induced current measurements.

Conductive, closed-loop sample induced currents were deter-mined at flux densities ranging from 0.6 μT to 16 μT with the R/C Loop and sample positioned at 7.62 cm and 5.72 cm from the HHC center, respectively. Due to a gradual decrease in the detected CW magnetic field strength during measurements, the average reference plane field strength measurements recorded immediately before and after removing the sample were used to calculate the field strength at the sample. The current amplitudes, $I_s(z)$, calculated using Eq. (5) for the large-radius, "thick-wire" samples listed in Table I at 65 MHz are shown in Fig. 7. The induced currents within each sam-ple linearly increased with an increase in flux density. The simi-larity of the results for the different materials indicates that in the evaluated closed-loop geometry, the induced current is insensitive to conductivity variation over a fairly large range (~1.5 orders of magnitude). This result is consistent with single small loop antenna theory which indicates that the current induced in a loop within a normal RF magnetic field is dominated by the radiation resistance rather than the ohmic losses in the loop for the conductivity range tested.[24]
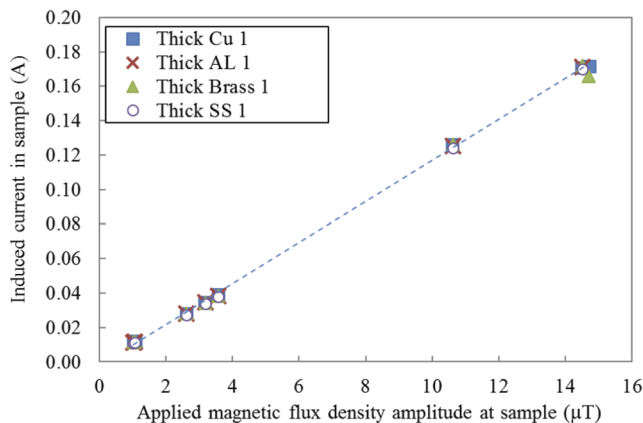

FIG. 8. Induced sample current amplitude for the thick Cu 1 sample at various frequencies vs measured magnetic flux density amplitude at 5.72 cm from the HHC center.

Figure 8 shows the experimental results of the large-radius, thick Cu 1 sample at 55 MHz, 65 MHz, and 85 MHz. The experi-mental data at 55 MHz were limited by the output level possible for the HHC at that frequency. Within the range evaluated up to ~4 μT, the results remained linear. The observed slopes for the 55 MHz and 85 MHz results are slightly lower than those at 65 MHz. This differ-ence may be due to the impedance differences of the closed loop at different frequencies or possibly parasitic effects (interference, capacitance, etc.) not included within the theoretical calculation.[24]

Figure 9 shows the currents induced by a 65 MHz, ~4 μT flux density for both the thin- and thick-wire Cu samples with differ-ent loop radii (thick Cu 1–Cu 3 and thin Cu 1–Cu 3 samples) along with the currents predicted by antenna theory for single-closed loop sizes of the same sized wires subjected to the same magnetic flux.[24]

FIG. 7. Induced sample current amplitudes for thick wire samples of various elec-trical conductivities located at 5.72 cm from the HHC center vs measured magnetic flux density amplitude at 65 MHz.
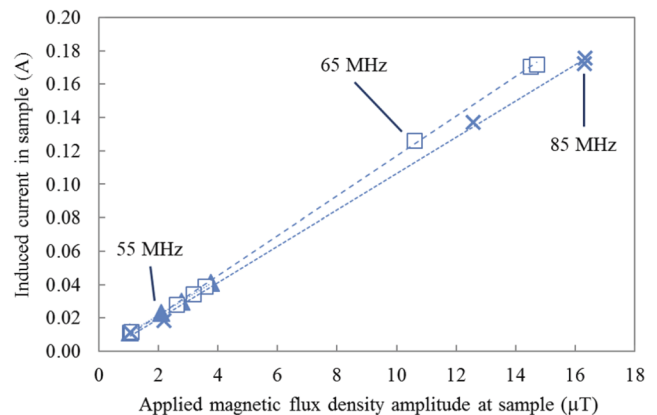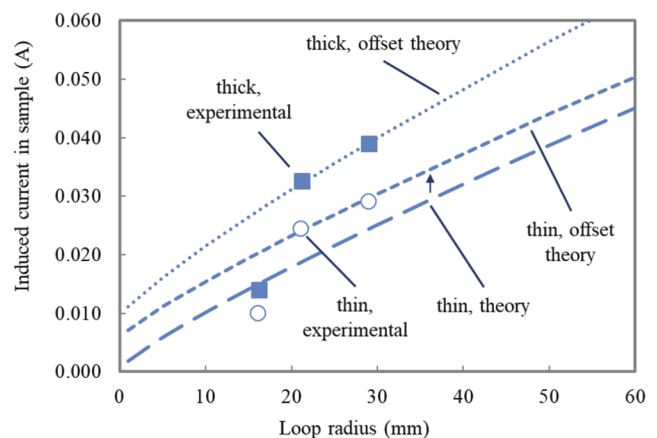

FIG. 9. Comparison of measured and loop impedance-based induced sample cur-rent amplitude results for copper wire samples of different wire diameters (thick Cu—0.50 mm with offset, and thin Cu—0.128 mm with and without offset) vs loop radius at ~4 μT magnetic flux density and 65 MHz located at 5.72 cm from the HHC center.
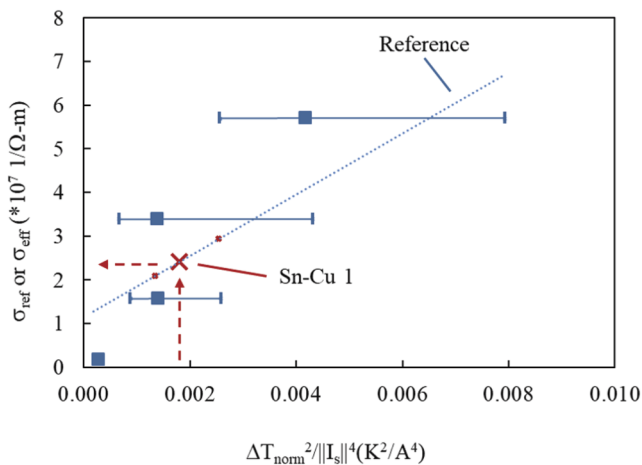
FIG. 10. Determination of the electrical conductivity vs the normalized temperature change/induced current ratio reference curve and estimation of effective conductivity prediction for the Sn-plated Cu thick wire sample.

For all loop sizes evaluated, the measured thick-wire induced current is higher than that for the thinner wire of the same size. This result matches antenna theory which indicates that the radiation impedance of a closed loop with a smaller wire diameter should be higher than that of the same sized loop made with thicker wire.[24] Offsetting the theoretical predictions to overlay the experimental results (0.0075 A and 0.0053 A for thick and thin, respectively) shows similar changes in induced current for the higher loop radius values measured but larger differences for the smaller loops, which showed better agreement without an offset applied. These differences are due to differences in the external impedance of the single loop theory compared to the measured loop within the concentric array.

Figure 10 shows the reference surface conductivity curve developed from the normalized temperature rise, ΔT_{norm}, and induced current measurement, $I_s(z)$. To enable averaging of temperature rise measurements recorded at different flux densities, the ΔT values are normalized by multiplying the measured temperature by the ratio of the squared average RF sample flux to the measured field. These values along with the calculated induced current values are provided in Table III.

The high variation shown in the reference curve developed from known material samples resulted from the limited accuracy of the temperature measurement technique utilized. The T/C tip to wire sample coupling efficiency was not optimal, and interference caused by the RF magnetic field in the T/C reader required the RF field to be deenergized during temperature measurements. The coupling efficiency issue can be resolved by using a more accurate thermal sensor attached to the wire sample with a more permanent, thermally efficient method (e.g., soldering). The interference issue requires the addition of low pass filtering in the T/Cs (or other temperature sensors) which inhibits the induced RF signal from reaching the temperature detection device. Despite these issues, the estimated effective surface conductivity value for the Sn-plated Cu wire material in the range of 2.09–2.94 × 10^7 1/Ω m is in good agreement with a previous study which analytically determined its effective conductivity value to be 2.99 × 10^7 1/Ω m; all values consistent with a skin depth consists of both Sn and Cu electrical conductivities.[25]

IV. SUMMARY AND CONCLUSIONS

A measurement system was developed utilizing EMC test equipment and antenna structures to produce similar inductive RF magnetic flux conditions like those existing within a 1.5 T MRI imaging system (MRI B_1) for use in the study of inductive behavior of non-magnetic, conductive materials. The derived experiment operates in continuous wave and pulsed wave modes and applies orthogonal RF magnetic fields to conductive, closed-loop samples in excess of 10 μT$_{rms}$ (14 μT$_{peak}$) at 65 MHz and 85 MHz. A superposition-based, analytical model enabling the distribution of the RF magnetic flux to be predicted from a single R/C loop voltage measurement at an HHC coaxial position, or reference plane, was derived and verified for reference plane selections outboard of the HHC loops. Using a similar modeling approach, a method for calculating the RF magnetic field strength at a sample location and the induced current within a conductive, closed-loop wire sample based on R/C loop voltage measurements was also demonstrated. Measurements taken using this approach show a linear relationship between the induced current and flux density up to 14 μT$_{peak}$ at 65 MHz. Changes in sample size and wire diameter and variations in electrical conductivity produced changes in the proportionality between the induced currents and flux density which matched antenna theory trends for a conductive, closed-loop geometry within a perpendicular RF magnetic field, providing additional validation of the measurement

TABLE III. Summary of average magnetic flux density at the sample, average normalized temperature rise, and induced current magnitude.

Sample	Average peak magnetic flux density at sample, B_{s-ave} (μT)	Average normalized temperature rise, ΔT_{norm} (°C)	Induced current magnitude, I_s (A)
Thick Cu 1	14.50 ± 0.16	0.5 ± 0.1	0.175 ± 0.003
Thick Al 1	14.42 ± 0.14	0.8 ± 0.4	0.172 ± 0.009
Thick brass 1	14.40 ± 0.21	0.8 ± 0.2	0.171 ± 0.004
Thick S.S. 1	14.39 ± 0.24	1.9 ± 0.1	0.169 ± 0.004
Thick Sn–Cu 1	14.41 ± 0.03	0.7 ± 0.1	0.176 ± 0.000

technique. Combining the induced current quantification with temperature rise measurements also demonstrated a means of determining effective surface EM properties. The quantification of induced current in conductive materials under RF magnetic fields utilizing this measurement system has the potential to accelerate advancement of material-based solutions to unintended RF magnetic field induced current related issues, like MRI/implanted device-related induction, because it provides a more accessible methodology for characterizing the effects of surface EM property modifying approaches. The measurement system is also scalable to other RF field conditions (e.g., 3.0 T MRI systems) by changing the HHC for the one optimized for the RF frequency of interest up to the limits of the small loop approximation. In combination with temperature rise measurements, induction measurements using the proposed measurement system can also be used for determining surface conductivity and/or permeability properties in material samples fabricated from unknown materials or with heterogeneous properties. The observed near field perturbation effect may also provide the basis of an imaging system that detects the spatially distributed attenuation in an RF magnetic field caused by a conductive object with an array of loop bolometers.[26] Future work will include improving the accuracy of temperature rise measurements to produce a more refined conductivity measurement method and additional development of the high RF field pulsed method.

DATA AVAILABILITY

The data that support the findings of this study are available from the corresponding author upon reasonable request.

REFERENCES

[1]D. A. Weston, *Electromagnetic Compatibility Principles and Applications* (Marcel Dekker, Inc., New York, NY, 1991), pp. 1–107.

[2]W. Graham and T. C. Tse Mo, IEEE Trans. Antennas Propag. **26**, 107 (1978).

[3]J. A. Nyenhuis, IEEE Int. Symp. Electromagn. Compat. **2**, 920 (2002).

[4]J. A. Nyenhuis, S.-M. Park, R. Kamondetdacha, A. Amjad, F. G. Shellock, and A. R. Rezai, IEEE Trans. Dev. Mater. Reliab. **5**, 467 (2005).

[5]A. Roguin, J. Schwitter, C. Vahlhaus, M. Lombardi, J. Brugada, P. Vardas, A. Auricchio, S. Priori, and T. Sommer, Europace **10**, 336 (2008).

[6]W. R. Nitz, A. Oppelt, W. Renz, C. Manke, M. Lenhart, and J. Link, J. Magn. Reson. Imaging **13**, 105 (2001).

[7]L. C. Van Dijk, J. Van Holten, B. P. van Dijk, N. A. A. Matheijssen, and P. M. T. Pattynama, Radiology **219**, 284 (2001).

[8]P. Nordbeck, G. Ertl, and O. Ritter, Eur. Heart J. **36**, 1505 (2015).

[9]V. Acikel, P. Magrath, S. E. Parter, P. Hu, H. H. Wu, J. P. Finn, and D. B. Ennis, J. Cardiovasc. Magn. Reson. **18**(1), O121 (2016).

[10]M. Elmaoglu, A. Celik, and M. Basak, *MRI Handbook: MR Physics, Patient Positioning, and Protocols* (Springer Science+Business Media, LLC., New York, 2012), pp. 7–17.

[11]F. G. Shellock and J. V. Crues, Radiology **232**, 635 (2004).

[12]A. Nowogrodzki, Nature **563**, 24 (2018).

[13]J. Nyenhius, J. Jallal, X. Min, S. Sison, and G. Mouchawar, Comput. Cardiol. **42**, 765 (2015).

[14]P. Nordbeck, I. Weiss, P. Ehses, O. Ritter, M. Warmuth, F. Fidler, V. Herold, P. M. Jakob, M. E. Ladd, H. H. Quick, and W. R. Bauer, Magn. Reson. Med. **61**, 570 (2009).

[15]O. Benafan, S.-Y. Chen, A. Kar, and R. Vaidyanathan, Rev. Sci. Instrum. **86**(12), 123903–123911 (2015).

[16]A. Kar and R. Vaidyanathan, "Surface modified materials for tailoring responses to electromagnetic fields," U.S. patent 2012/0296350 A1 (22 November 2012).

[17]ASTM F2182-11a, Standard Test Method for Measurement of Radio Frequency Induced Heating on or Near Passive Implants During Magnetic Resonance Imaging, ASTM International, West Conshohocken, PA, 2011.

[18]M. V. Vaidya, C. M. Collins, D. K. Sodickson, R. Brown, G. C. Wiggins, and R. Lattanzi, Concepts Magn. Reson., Part B **46**, 25 (2016).

[19]J. Lindsay, IEEE Trans. Antennas Propag. **15**, 697 (1967).

[20]See http://www.schwarzbeck.com/appnotes/EMIRcvrCISPR16.pdf for the EMI-Receiver. According to CISPR 16-1-1., Schwarzbeck Application Notes by D. Schwarzbeck.

[21]R. E. Collin and F. J. Zucker, *Antenna Theory: Part 1* (McGraw-Hill Book Company, New York, NY, 1969), pp. 458–482.

[22]F. M. Greene, J. Res. Natl. Bur. Stand., Sect. C **71C**, 319 (1967).

[23]A. Barletta and E. Zanchini, Wärme - und Stoffübertragung **29**, 285 (1994).

[24]*Antenna Engineering Handbook*, 4th ed., edited by J. L. Volakis (McGraw-Hill, New York, NY, 2007), pp. 5-1–5-20.

[25]J. M. Jennings, R. Vaidyanathan, and A. Kar, J. Appl. Phys. **125**, 035106 (2019).

[26]A. Kar, R. Vaidyanathan, and J. M. Jennings, "Cost-effective imaging system uses RF magnetic field and loop bolometer array to produce MRI-quality images," patent pending (2019).